



Rheological characterization of viscoplastic fluid flow in a pipe with wall slip using in situ particle image velocimetry

Yamid J. García-Blanco¹ · Vitor Y. Urazaki¹ · Ángel. D. J. Rivera¹ · Luis H. Quitian¹ · Eduardo M. Germer¹ · Admilson T. Franco¹

Received: 24 May 2022 / Revised: 5 October 2022 / Accepted: 4 November 2022 / Published online: 16 December 2022
© The Author(s), under exclusive licence to Springer-Verlag GmbH Germany, part of Springer Nature 2022

Abstract

The current experimental study investigates the rheological characterization of Carbopol gel solutions into a pipe flow using in situ visualization. The shear rate and shear stress profiles for different pressure-driven values are presented and correlated to obtain new steady-state flow curves compared with rheometrical data performed with cross-hatched parallel plate (CHPP) and smooth concentric cylindrical (SCC) geometries at a rotational rheometer. The rheological behavior for the test performed by the in situ visualization was well fitted by the generalized Herschel-Bulkley model, and different values for the coefficient of consistency (K), flow behavior index (n), and yield stress (τ_0) were fitted for the three gel solutions due to the presence of wall slip behavior. The discrepancies between the values of the rheological parameters suggest that conventional rheometrical measurements, which avoid the slippage of the fluid, lead to an overestimation of these parameters, and as a consequence, these discrepancies are extended to the dimensionless numbers calculated for the hydrodynamic flow description. Also, the experimental plug core velocity was compared with the analytical value obtained by the rotational rheometer tests to calculate an equivalent slip velocity, and such velocity depicts a quasi-linear trend with the wall shear stress. This is supported by the apparent viscosity profiles along the pipe diameter, suggesting that the slippage is an inherent characteristic of polymer gel solutions, and it is disseminated by the presence of layers near the pipe wall where the Newtonian like-behavior is presented. Finally, applying in situ visualization technique assures a better rheological characterization and accurate description of the flow conditions for fluids with complex behavior.

Keywords Viscoplastic fluid · Rotational rheology · Flow curve · Carbopol solutions · Slip behavior · PIV

Introduction

The rheology of complex fluids has been studied for decades due to its relevance for understanding their behavior in industrial processes and natural phenomena (Di Giuseppe et al. 2015). In this context of complex fluids, there is a group of materials that require minimum shear stress to flow; these materials are known as viscoplastic fluids and

are used in broad processes such as drilling activities in the oil and gas industry (Caenn et al. 2011), particle and slurries transportation (Ghàitanellis et al. 2018; Turian and Yuan 1977; Mika 2012), food products, and fill molding processes (Coussot et al. et al. Dusunceli and Colak 2008). The viscoplastic fluids present shear-thinning behavior, and the minimum shear stress requirement is due to the presence of yield stress, which dominates the transition of the material from a gel-like to an unstructured condition (Bonn et al. 2017; Fernandes et al. 2017b). Some experimental studies have focused on the measurements of the rheological parameters of viscoplastic materials, particularly to determine the yield stress value (De Graef et al. 2011; Mendes et al. 2017; Fernandes et al. 2021). Nevertheless, there is a disagreement between the different methods and devices used to evaluate the rheological properties of viscoplastic materials (Fernandes et al. 2019).

Rotational rheometers (Mahto and Sharma 2004), Couette viscosimeters (Bourgoyne Jr et al. 1986), and capillary

Vitor Y. Urazaki, Ángel. D. J. Rivera, Luis H. Quitian, Eduardo M. Germer, and Admilson T. Franco contributed equally to this work.

✉ Yamid J. García-Blanco
yamidblanco@alunos.utfpr.edu.br

✉ Admilson T. Franco
admilson@utfpr.edu.br

Extended author information available on the last page of the article.

rheometry (Li and Wolcott 2005) are the most common methodologies used for the rheological analysis and characterization of complex fluids. Measurements to determine the steady-state flow curve for viscoplastic fluids are usually performed to characterize the rheological behavior, and the flow curves are commonly fitted using the widespread general Herschel-Bulkley model. This model is suitable for polymer solutions since it can be reduced to Bingham or Power-law model according to the value of its variables (Kim et al. 2003; Zhu et al. 2005). The general Herschel-Bulkley model is described for the shear stress as

$$\tau = \tau_0 + K \dot{\gamma}^n, \quad \tau > \tau_0 \quad (1)$$

where τ_0 is the yield stress, and K and n are the coefficient of consistency and the flow behavior index, respectively. Note that the Eq. 1 is valid just for $\tau > \tau_0$, for the condition where $\tau < \tau_0$ then $\dot{\gamma} \rightarrow 0$ (Tanner 2000; Chhabra and Richardson 2011).

Commonly, cross-hatched parallel plate (CHPP) geometry is employed at the rheometer to perform the steady-state flow curve due to the roughness on the wall plate surface preventing the slipping of shear-thinning materials (Dimitriou et al. 2011). Instead, other geometries such as smooth concentric cylinders (SCC) and smooth parallel plate (SPP) are employed to perform rheometric measurements at high shear rates (Fernandes et al. 2017a), conditions where the slipping behavior at the wall geometry is reduced.

Experimental studies such as the ones by Pérez-González et al. (2012) and Aktas et al. (2014) visualized and quantified the slippage effect on the wall surfaces using rotational and pressure-driven flows by parallel plate geometries and capillary rheometric configurations. Previous results suggest the existence of a slipping velocity, which is directly correlated with the decrease of the wall shear stress. Also, these experimental studies have allowed a better insight into the viscoplastic flow for pipeline setups by using different visualization techniques.

Most experimental studies have suggested and recommended methodologies to correct the shear rate to find a “real flow curve” for replicating the data obtained with rheometrical tests under non-slipping conditions such as Schmidt et al. (1999), Fernandes et al. (2019), Cheng (1986), and Pérez-González et al. (2012). Although widely used in the study of the rheological properties of viscoplastic fluid, only a few works in the literature have analyzed the accuracy of these correction methodologies, comparing them with flow kinematics measurements (Kalyon et al. 1993; Aktas et al. 2014), such as the Weissenberg-Rabinowitsch equation (Yoshimura and Prud'homme 1988; Macosko 1994). Since the slip behavior is an inherent characteristic of viscoplastic fluids (Jiang et al. 1986; Schmidt et al. 1999; Piau 2007) and affects the flow kinematics, especially in pipe flow (Peixinho et al. 2005; Sobamowo

et al. 2018; Koponen et al. 2019; García-Blanco YJ et al. 2021), better characterization and evaluation of the rheological properties of pipeline viscoplastic fluid flow with non-conventional methodologies are demanded.

In situ flow visualization techniques are generally developed with Rheo-PIV arrangements, which require expensive and complex devices such as capillary tubes and control temperature equipment (Marín-Santibáñez BM et al. 2020; Younes et al. 2021; Medina-Bañuelos et al. 2022). Despite the significant advances in the visualization of flow with slip behavior and the methodologies for slippage correction of rheometrical data, few works have performed rheological characterization of viscoplastic fluids with similar conditions to the industrial performance where these types of fluids are employed (Andrade et al. 2016; de Oliveira and Negrao 2015). Therefore, the present study investigates laminar steady-state flows of three viscoplastic Carbopol solutions using in situ PIV in a pipeline flow loop. Shear strain calculations are conducted based on the velocity gradient correlations and used to determine in situ shear rate and shear stress profiles by the imposition of different pressure drop values along the test section.

This paper outlines the methodology to obtain rheological parameters (K , n , and τ_0) from in situ flow curves for viscoplastic fluids, which are evaluated by the comparison of the analytical plug core velocity calculations with the data obtained from the experimental velocity profiles, demonstrating suitability for such flow measurements. Also, the technique developed here is based on a conventional PIV setup, simplifying the process and the analysis of the slipping behavior for polymer solution with reasonable accuracy. The experimental performance is focused on developing the study in devices with similar dimensions to the equipment employed in industrial processes such as the start-up of oil after a flow cessation inside pipelines in offshore exploration, where a good accuracy characterization of the slip velocity is reached, and a relationship with the increase of the wall shear stress is also presented and compared with the data available literature.

Materials and methods

Fluids preparation

For the experimental studies developed in this article, aqueous solutions of Carbopol at 25 °C were prepared by dissolving a commercial ultrasound gel (RMC ind., Brazil) composed of ~0.4 wt% of Carbopol 940 (carboxyvinyl polymer) in distilled water to guarantee chemical stabilization (Muramatsu et al. 2000; Chun and Choi 2004; Piau 2007; Shamu et al. 2020). The mixtures were stirred for at least 12 h to guarantee a homogeneous final composition

and then were maintained at rest for another 12 h. The pH was adjusted via neutralization with sodium hydroxide (NaOH) solution with 18 wt% under agitation, and monitored using a digital pH-meter (Quimimis, Brazil) until it reached a neutral pH between 7.2 ± 0.1 . Final Carbopol concentrations of 0.08 wt%, 0.12 wt%, and 0.16 wt% were obtained and named C1, C2, and C3 for better identification issues.

For validation of the PIV methodology, a Newtonian fluid was employed. A 50 wt% glycerin solution with distilled water was prepared and stirred for 2 h to guarantee proper homogenization. The Newtonian solution did not require any stabilization or neutralization during the preparation stage, and it was kept at rest for 6 h before usage. The different fluids prepared are listed and identified in Table 1.

Rheometrical measurements

The rheometrical tests were conducted in a stress-controlled rotational rheometer Haake MARS III (Haake Thermo Scientific, Germany), which is capable of measuring a minimum rotational torque of $0.01 \mu\text{Nm}$ and a maximum torque of 0.2 Nm with a resolution of 0.1 nNm, respectively, and has a maximum uncertainty lower than 5% of the reading (Longo and Zilio 2011; Andrade et al. 2016; Quitian et al. 2022). The rheometer controlled the temperature of all tests at 25 °C by a Peltier system assisted by a thermostatic bath.

Two different geometries were employed in the experiments with the Carbopol solutions. A 35-mm diameter cross-hatched surface parallel-plate geometry (CHPP) with a 1-mm gap to avoid wall slip (Dimitriou et al. 2011; Zhang et al. 2018), and a smooth Couette geometry (internal cylinder diameter of 25 mm, length of 40 mm, cup diameter of 26 mm, and 0.51 mm groove depth). Further, a 40-mm diameter smooth parallel plate (SPP) with a 0.8-mm gap was used to characterize the glycerin solution.

Figure 1(a) and (b) depict the schematic representation of the parallel plate and concentric cylinder geometries used for performing rotational rheometry tests. In both geometries, one of the walls is in contact with the fluid and spins while the other one is maintained fixed. For the case of the parallel plate configuration, the upper plate spins at a controlled velocity, and the lower plate is fixed instead. In the case of the concentric cylinder configuration,

the outer cylinder is fixed, and the inner one spins with a controlled rotation. The velocity field in the gap between the walls in both geometries can be analyzed thoroughly as unidirectional flow, characterized by a linear profile and a high-velocity gradient. The shear rate in the whole gap is calculated and used for correlating the shear stress as a response to the shear rate imposed on the fluid.

Steady-state flow curves for Carbopol solutions were conducted by imposing a series of constant shear rates. Measurements made with CHPP had shear rate levels ranging from 0.01 to 1100 s^{-1} for 600 s each shear rate, which is enough time for the material to reach the steady-state regime. For the SCC geometry, the shear rates were from 1 to 1100 s^{-1} , with the same duration per shear rate. The measurements for the glycerin solution were carried out by applying a descending shear rate ramp in the range between 1 and 100 s^{-1} . Before each experiment, the Carbopol solutions (C1, C2, and C3) were presheared at 5 s^{-1} over 120 s; after, the sample was kept left under a zero-shear stress condition for 180 s. All the rheometric measurements were conducted in triplicate, each test was performed with fresh sample in order to avoid fluid degradation and evaporation, and also to guarantee statistical accuracy. Figure 2(a) shows the flow curve obtained for the three Carbopol and glycerin solutions, and the fit of the rheometric data by the Herschel-Bulkley model. Carbopol solutions display a shear-thinning behavior with a dynamic yield stress, which increases with the weight concentration. The confidence interval at low shear rate values is presented for the Carbopol solutions in Fig. 2(a)–(c). The band width of the confidence interval is lower for the more concentrated Carbopol solutions, due to the low deviation of the data for low shear rates. However, the band width and the low values of the error bars show a satisfactory performance of the rheometric tests.

The SCC geometry presents a reduction of the yield stress for the three Carbopol solutions. The latter supports that there is a significant slippage behavior for this geometry. For glycerin solution (G50) presented Newtonian fluid behavior with a dynamic viscosity of $6.32 \times 10^{-3} \text{ Pa}\cdot\text{s}$. Table 2 summarizes the fitted parameters of the Herschel-Bulkley model and the physical properties of each fluid.

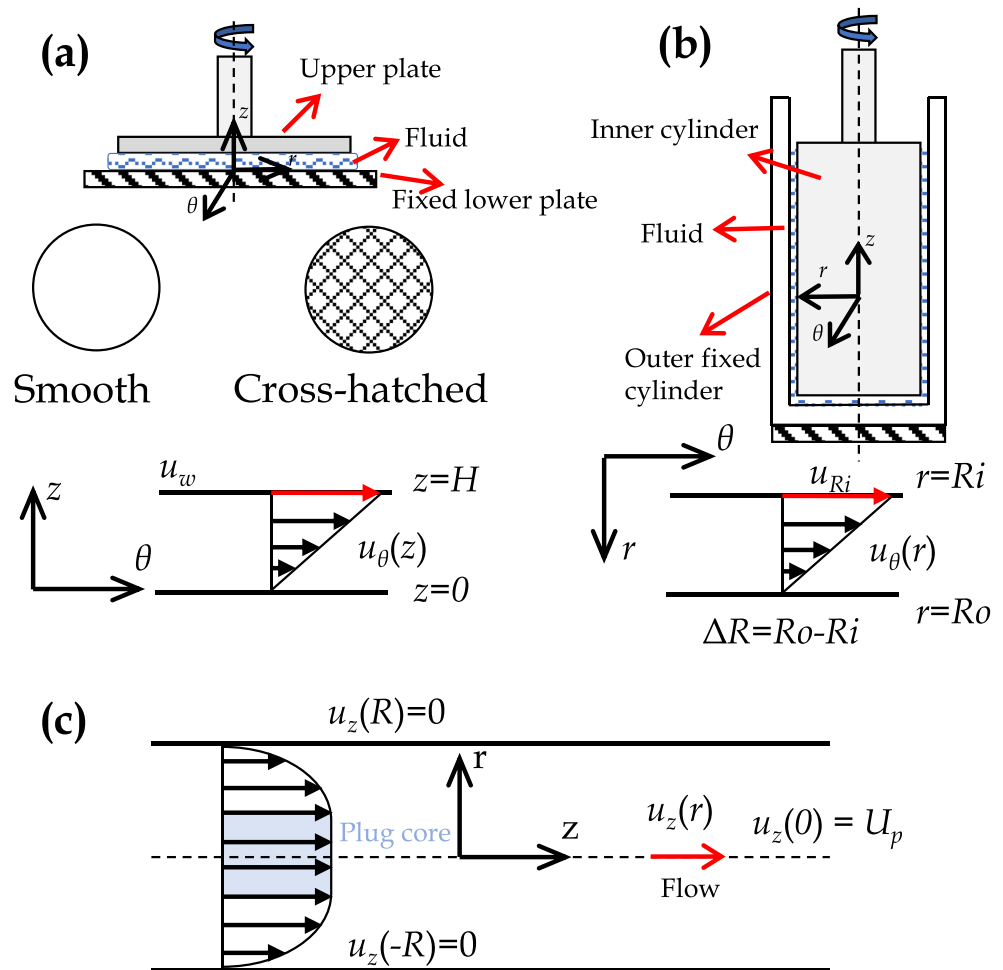
Experimental setup and apparatus arrangement for visualization

The flow loop facility of length 12.5 m is presented in Fig. 3. The test section consists of an acrylic assembly of a solid transparent, straight pipe inside a box filled with water, providing optical access for flow visualization. The flow loop facility has pipes with an internal diameter (D) of 25.9 mm. The fluid was contained in a 100-l tank (i) provided with a mixing system for homogenization. The

Table 1 Fluids and concentrations used in this study

Fluid name	Type of fluid	Concentrations
C1	Carbopol	0.08wt%
C2	Carbopol	0.12wt%
C3	Carbopol	0.16wt%
G50	Glycerin	50wt%

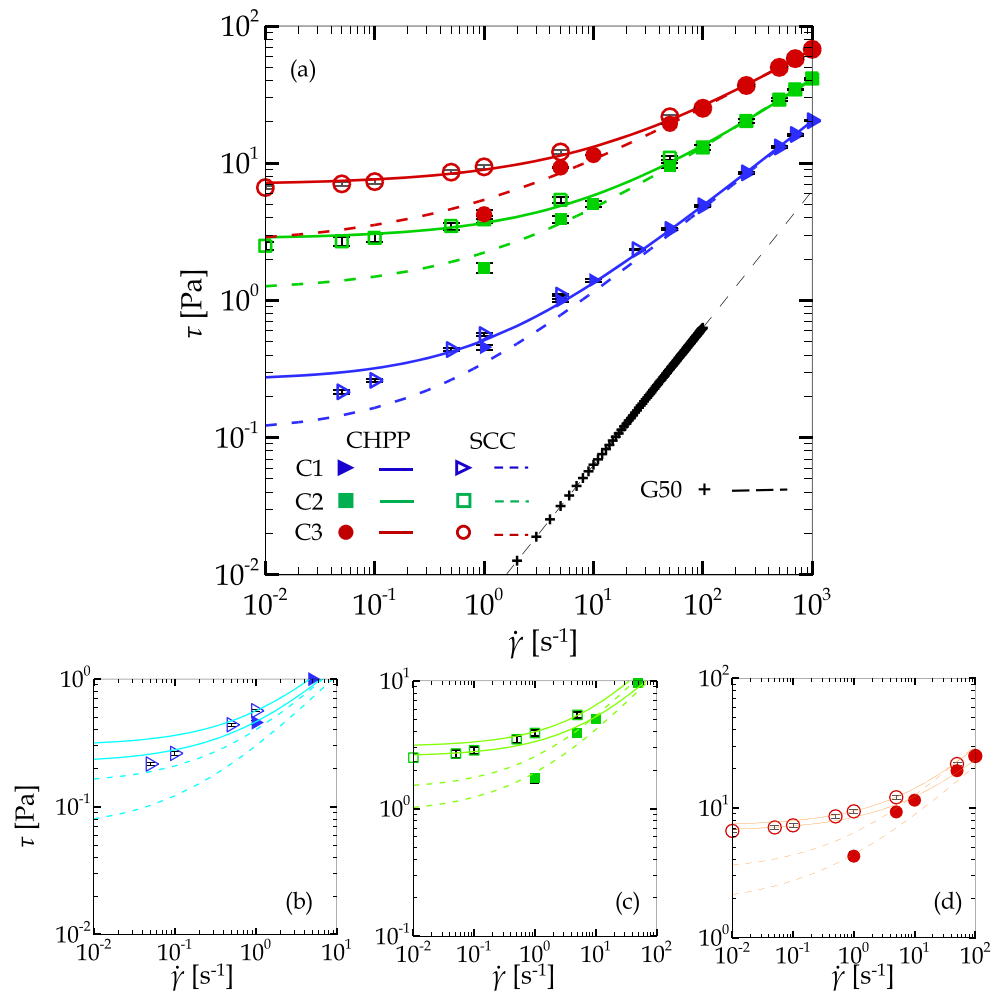
Fig. 1 Schematic representations of the typical geometries employed for rotational rheometric tests and the velocity distribution for a theoretical viscoplastic pipe flow. Schema of typical (a) cross-hatched and smooth parallel-plate geometries and (b) smooth concentric cylinders. (c) Schema of a typical velocity profile for a viscoplastic material into a pipeline



fluid was homogenized before running each experiment, and the flow was provided by a helical rotor mono pump of 3 HP (ii). The pump was controlled by a variable-frequency inverter (iii) with a mass flow meter (iv); temperature and density were measured also by the mass flow meter as secondary outputs. The error of the mass flow meter upon the mean flow rate was estimated as $\pm 1\%$. Two pressure transmitters (vi) obtained pressure measurements, and they were connected to the measure points 1, 2, and 3, with a distance of 1 m between them. The gauge pressure transmitter at point 1 controls the entrance conditions into the test section to prevent over-pressure in the flow loop, and the differential pressure transmitter measures the pressure drop at points 2 and 3, before and after the test section (v), respectively. Pressure tappings with 4 mm of internal diameter were connected to the pressure transmitters by cylindrical tubes filled with de-ionized water to avoid pH modifications of the fluid and erroneous pressure measurements. The pressure transmitters error was estimated at $\pm 0.1\%$ for the span range (0–62 mbar), and $\pm 0.4\%$ for a full measurement range (until 138 bar).

The experimental setup for the PIV system is schematically illustrated in Fig. 4(a). It consists of a double-pulsed laser of 60 mJ (Nano-L-50-100) (8) and a wavelength of 532 nm with an optical lens (10). The laser was synchronized with a CCD camera (7) (Hi-Speed Nano Sense MK III) and a Nikon AF Micro Nikkor 60 mm $f/2.8D$ lens (9). The laser sheet (11) was aligned at 90 degrees to the camera plane, with 1 mm of thickness. According to the flow conditions, the data acquisition was set at 100 Hz, and the time between pulses varied from 50 to 650 μs . The camera has 4 GB of onboard memory, able to achieve 1040 pairs of images at 1280×1024 pixels of maximal resolution. Laser reflections were filtered with a 570-nm optical filter mounted on the camera lens. Polyamide particles coated by Rhodamine-B and an average diameter of 10 μm were used as seeding particles. The Dynamic Studio software (Dantec Dynamics A/S) was employed to control the data acquisition and the further process correlation of the acquired images. Figure 4(b) shows the straight pipe test section dimensions scaled by the internal pipe diameter, defined as $D \times 2D$, its dimensions are chosen to be large enough to

Fig. 2 (a) Steady-state flow curve for Carbopol solutions C1, C2, C3, and G50 Newtonian fluid, along with the best fit by the Herschel–Bulkley model. Empty and filled symbols are the rheometrical data obtained with CHPP and SCC geometries, respectively. Rheometrical data for Newtonian fluid G50 was fitted by the Newtonian model, represented by the long-dashed line. Bandwidth of the confidence interval for each Carbopol solution: (b) C1, (c) C2, and (d) C3. Error bars show the standard deviation of the rheometric tests performed in triplicate



ensure a good description of the flow behavior. The sampling error of the PIV technique associated with the flow statistics measurements is obtained by estimating an equivalent measure time (M_t) expressed in integral time scales (I_t). M_t is estimated by the size of the area visualized in the axial direction multiplied by the number of recorded images and then divided by the mean velocity of the flow, $M_t =$

$2D \times N_i / U$; the integral time may be estimated by dividing the pipe diameter by the mean velocity, $I_t = D/U$. According to Westerweel et al. (1996), the sampling error for the flow statistics is inversely proportional to the square root of the measuring time expressed in integral times scales, $e_s = 1/\sqrt{N_i}$; where N_i is the total number of recorded images. Then, the current visualization setup yields a

Table 2 Density (ρ) and Herschel-Bulkley model parameters fitted for the Carbopol solutions

Fluid	ρ [Kg/m ³]	Fitted parameters						
		CHPP			SCC			SPP
		τ_0 [Pa]	K [Pa·s ^{<i>n</i>}]	n [-]	τ_0 [Pa]	K [Pa·s ^{<i>n</i>}]	n [-]	μ [Pa·s]
C1	997.32	0.262 ± 0.040	0.251 ± 0.010	0.634 ± 0.006	0.11 ± 0.042	0.24 ± 0.008	0.64 ± 0.004	–
C2	997.44	2.821 ± 0.252	0.85 ± 0.0752	0.551 ± 0.013	1.178 ± 0.2488	1.054 ± 0.075	0.527 ± 0.010	–
C3	997.75	6.994 ± 0.327	1.975 ± 0.153	0.495 ± 0.011	2.53 ± 0.724	2.88 ± 0.297	0.451 ± 0.014	–
G50	1150	–	–	–	–	–	–	6.32e-3 ± 3.53e-6

The G50 solution is a Newtonian fluid; the dynamic viscosity (μ) value was fitted using the linear Newton’s correlation. For Newtonian fluid, τ_0 and n are considered as 0 and 1, respectively; μ is the equivalent variable for K in Newtonian fluids

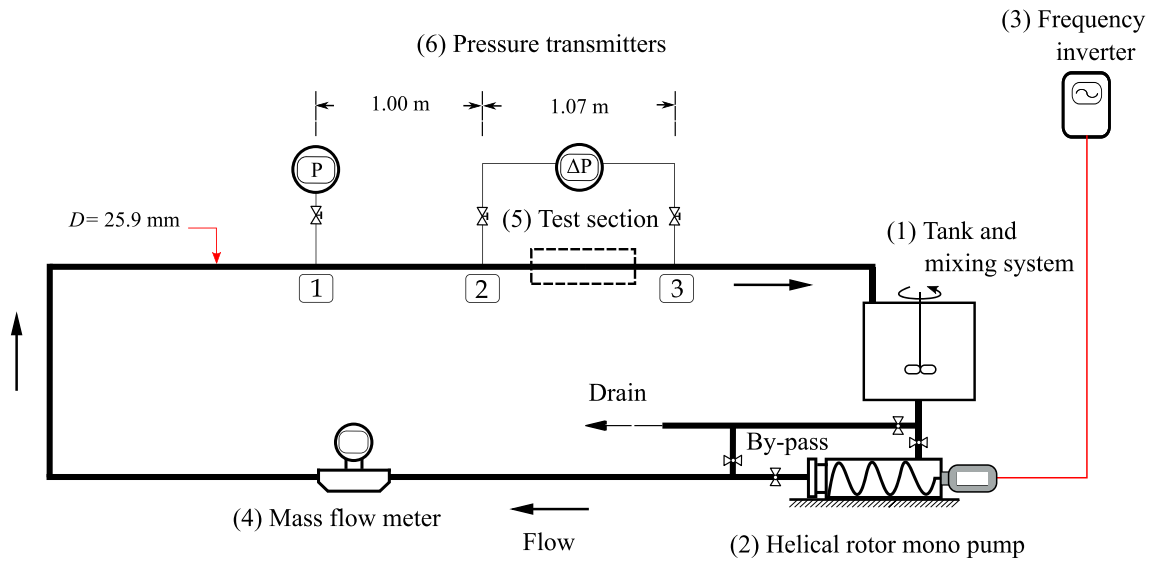


Fig. 3 Schematic diagram of the flow loop facility

sampling error of 2.2%. The processing stage of the images was performed using interrogation areas of 32×32 with overlapping of 50%, obtaining a vector point each 0.432 mm (1 pixel \sim 0.027 mm).

Velocity, shear rate, and shear stress calculation

The velocity fields were obtained by comparing the velocity neighbor vectors to one another. The central difference scheme was used to compare an interrogation area located at a given position m, n with its neighbors in $m, n + 1$ and $m, n - 1$ (Raffel et al. 1998). If only one velocity neighbor vector can be found, a forward or backward difference

schema is used instead, and the interrogation area in m, n is compared with the neighbor $m, n + 1$ or $m, n - 1$ (Raffel et al. 1998). Both difference schemas are presented in Fig. 5 with a simple representation.

The velocity gradient of the axial component u in the z -direction is calculated by the spatial correlation of the interrogation area located at position (m, n) , with its neighbors as:

$$\frac{\partial u}{\partial z}(m, n)_{central} \cong \frac{u_{m+1,n} - u_{m-1,n}}{z_{m+1,n} - z_{m-1,n}} = \frac{u_{m+1,n} - u_{m-1,n}}{2\Delta z} \tag{2}$$

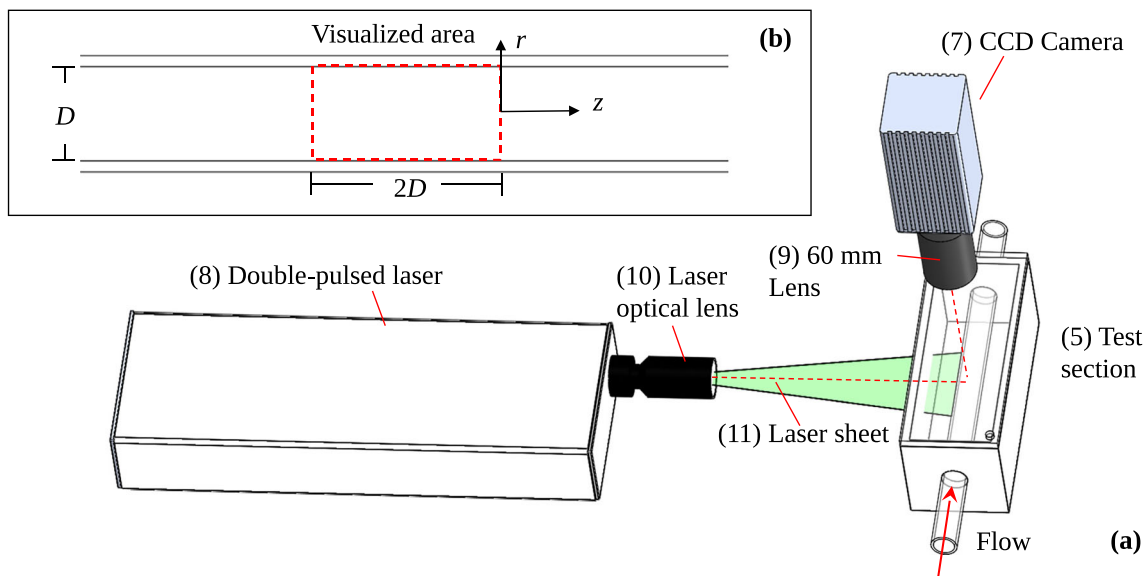


Fig. 4 Experimental setup for image visualization: (a) PIV technique components; (b) detailed view of the visualization area dimensions as a function of the internal pipe diameter (D)

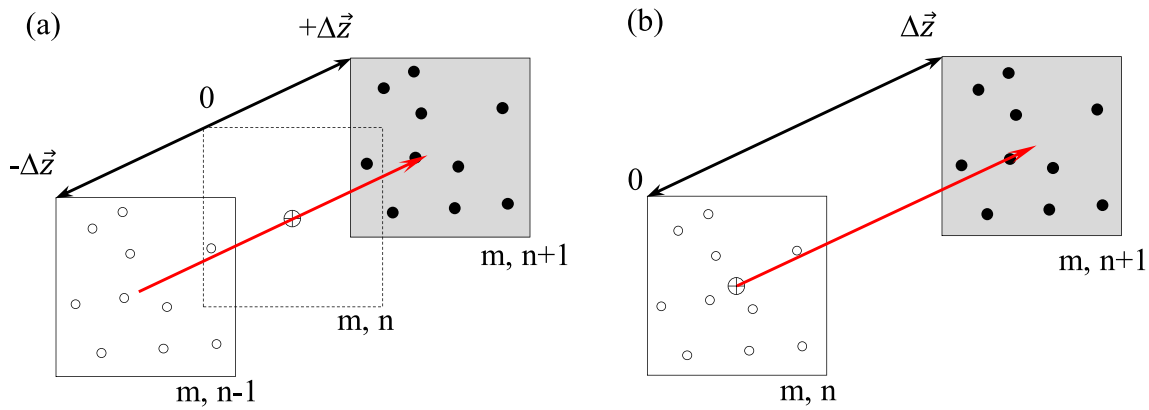


Fig. 5 (a) Central and (b) forward/backward different schemes for the calculation of the velocity and velocity gradients. The calculations are generated by correlating the seeding particles displacement along the visualized section during two image frames. The position m, n is the

interrogation area under analysis. According to the scheme applied, the interrogation area is correlated with the neighbors located at positions $m, n + 1$ and $m, n - 1$ (Raffel et al. 1998)

The results of the velocity gradients calculated by the central difference scheme correspond to the slope of a second-order polynomial fit to three neighbor velocities and are thus a second-order accurate. If there are only two valid neighbors, the forward or backward difference scheme can be applied:

$$\frac{\partial u}{\partial z}(m, n)_{forward} \cong \frac{u_{m+1,n} - u_{m,n}}{z_{m+1,n} - z_{m,n}} = \frac{u_{m+1,n} - u_{m,n}}{\Delta z} \quad (3)$$

$$\frac{\partial u}{\partial z}(m, n)_{backward} \cong \frac{u_{m+1,n} - u_{m,n}}{z_{m+1,n} - z_{m,n}} = \frac{u_{m+1,n} - u_{m,n}}{\Delta z} \quad (4)$$

In this case, forward and backward difference schemes correspond to the slope of first-order polynomial fits to two neighbor velocities and are first-order accurate.

Velocity vector field maps were obtained after the statistical analysis of the correlated values. These vector field maps furnished information on the mean axial velocity and the velocity gradients.

The shear rate tensor is derived from the velocity gradients calculation (Raffel et al. 1998), which is expressed in cylindrical polar coordinates by:

$$\hat{\gamma} = \left(\frac{1}{r} \frac{\partial u_r}{\partial \theta} + \frac{\partial u_\theta}{\partial r} - \frac{u_\theta}{r} \right) \hat{e}_r + \left(\frac{\partial u_\theta}{\partial z} + \frac{1}{r} \frac{\partial u_z}{\partial \theta} \right) \hat{e}_\theta + \left(\frac{\partial u_r}{\partial z} + \frac{\partial u_z}{\partial r} \right) \hat{e}_z \quad (5)$$

where each term describes the shear parallel to the $r\theta$ -, θz -, and rz -planes, respectively. However, for the planar projection of the visualized area by the PIV technique,

only the shear rate values parallel to the rz -plane can be determined as (Reuss et al. 1989; Raffel et al. 1998):

$$\dot{\gamma}_{rz} = \frac{\partial u_r}{\partial z} + \frac{\partial u_z}{\partial r} \quad (6)$$

The shear stress distribution was calculated using the linear wall shear stress relationship (Katritsis et al. 2007)

$$\frac{\tau_w}{\tau_{rz}} = \frac{R}{r} \quad (7)$$

where τ_{rz} is the local shear stress along the pipe diameter. The wall shear stress was calculated using the extension of the Hagen-Poiseuille formula (Katritsis et al. 2007; Wilms et al. 2020)

$$\tau_w = \frac{\Delta P_{2-3} D}{4L_{2-3}} \quad (8)$$

where pressure drop values ΔP were measured with the differential pressure transmitter placed in the test section at points 2 and 3, as indicated in Fig. 3. The pressure drop was increased with the flow rate imposed by the pump into the flow loop. The laminar and fully developed flow was guaranteed with a constant pressure drop behavior during the flow and a large relatively $L/D = 115$, where L is the entrance length of the flow loop before the test section.

Results

Figure 1(c) shows a schematic representation of a pressure-driven flow of a viscoplastic material in a pipeline configuration. The viscoplastic fluids depict a central unyielded plug region, where the shear stress does not exceed the material's yield stress, and this region is delimited by $r = r_0$, where r_0 is the radius of the central plug. The axial

Fig. 6 Comparison of the axial velocity profiles obtained from rheological parameters measured with a rotational rheometer Haake MARS III with parallel plate geometry and the experimental data obtained by the Particle Image Velocimetry technique of a Carbopol solution. On the *left side* is presented the velocity profile for a pressure drop of 244 Pa. The *right side* depicts the velocity profile after increasing the pressure drop value to 643 Pa. The zoom region shows a non-zero velocity depicted at the pipe wall by the PIV data for both cases. Error bars present the deviation for each point measured by the PIV technique

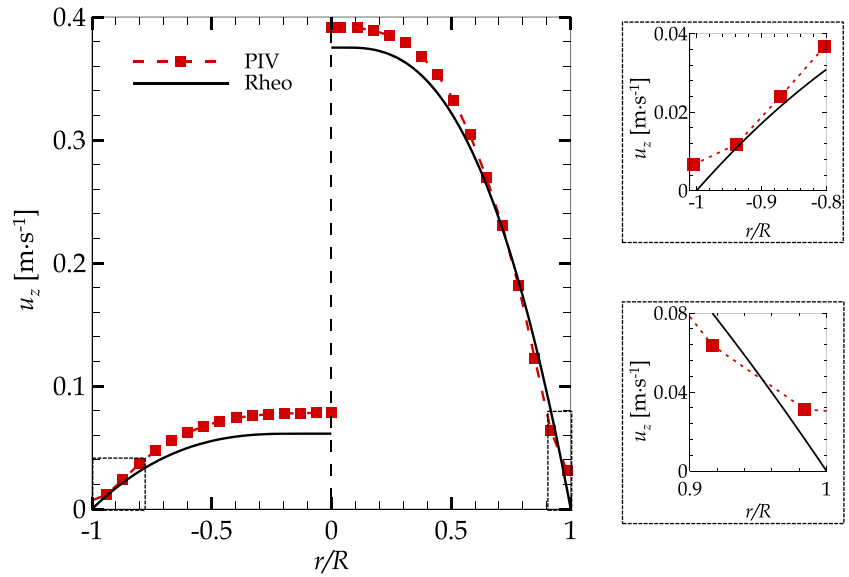
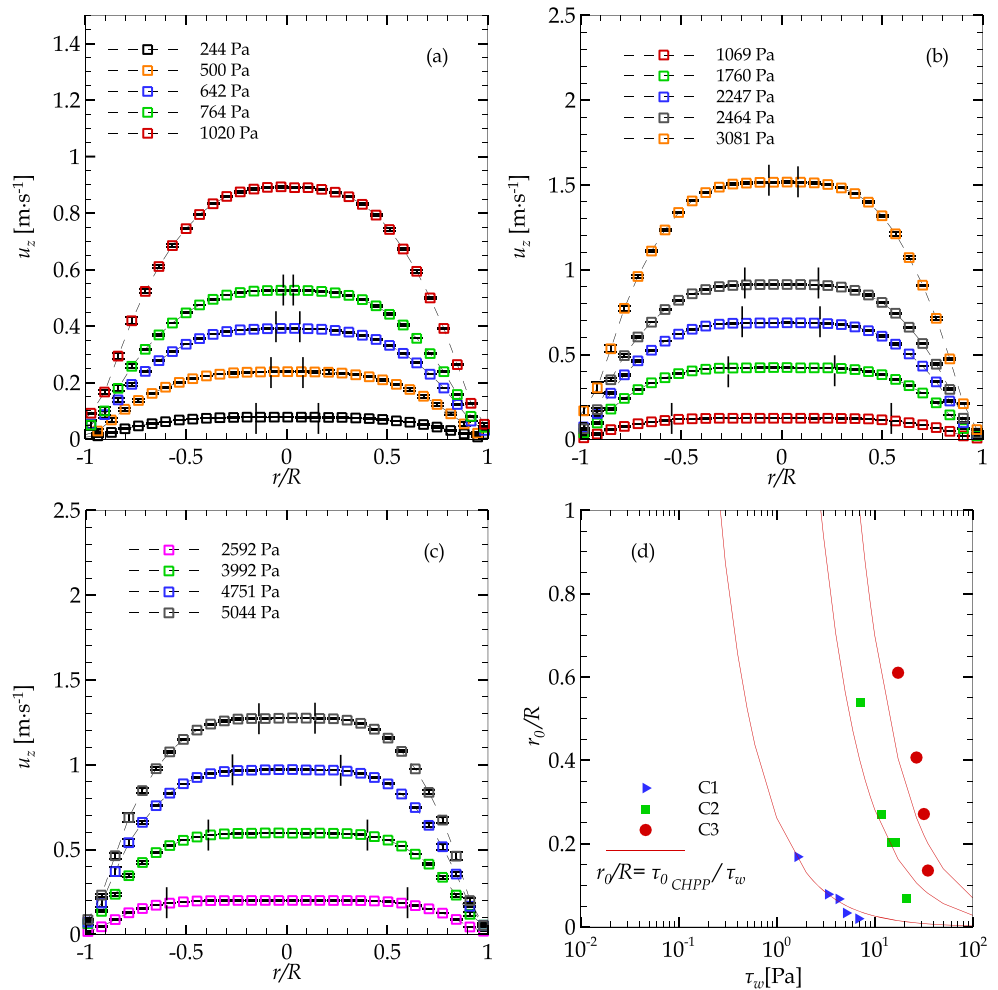


Fig. 7 Axial velocity profiles for different driven pressures: (a) C, (b) C2, and (c) C3; the dashed lines represented the radius of the plug region, r_0 . (d) The size of the plug radius as a function of the wall shear stress is presented; the visualized plug radius by the PIV methodology is compared with the shear stress–yield stress ratio obtained from the rheometric test with the CHPP geometry, represented by the red solid lines



velocity profile for pressure-driven flow configuration is then given by Chhabra and Richardson (2011)

$$u_z = \left(\frac{nR}{n+1} \right) \left(\frac{\tau_w}{K} \right)^{1/n} \left[(1-\phi)^{(n+1)/n} - \left(\frac{r}{R} - \phi \right)^{(n+1)/n} \right] \tag{9}$$

where ϕ is the ratio between the yield stress and the wall shear stress (τ_0/τ_w); this ratio can be also expressed as the ratio r_0/R .

Figure 6 compares the analytical axial velocity profile obtained with the rheological data measured in the rotational rheometer Haake MARS III with parallel plate geometry, and the data obtained with Particle Image Velocimetry (PIV) visualization of a pressure-driven flow into a pipeline configuration.

Noticeable differences in the velocity profiles are depicted for the plug core region. Near the wall, a non-zero velocity is also depicted by the PIV technique, supporting the presence of slipping movement at this region, which affects the final velocity measurements.

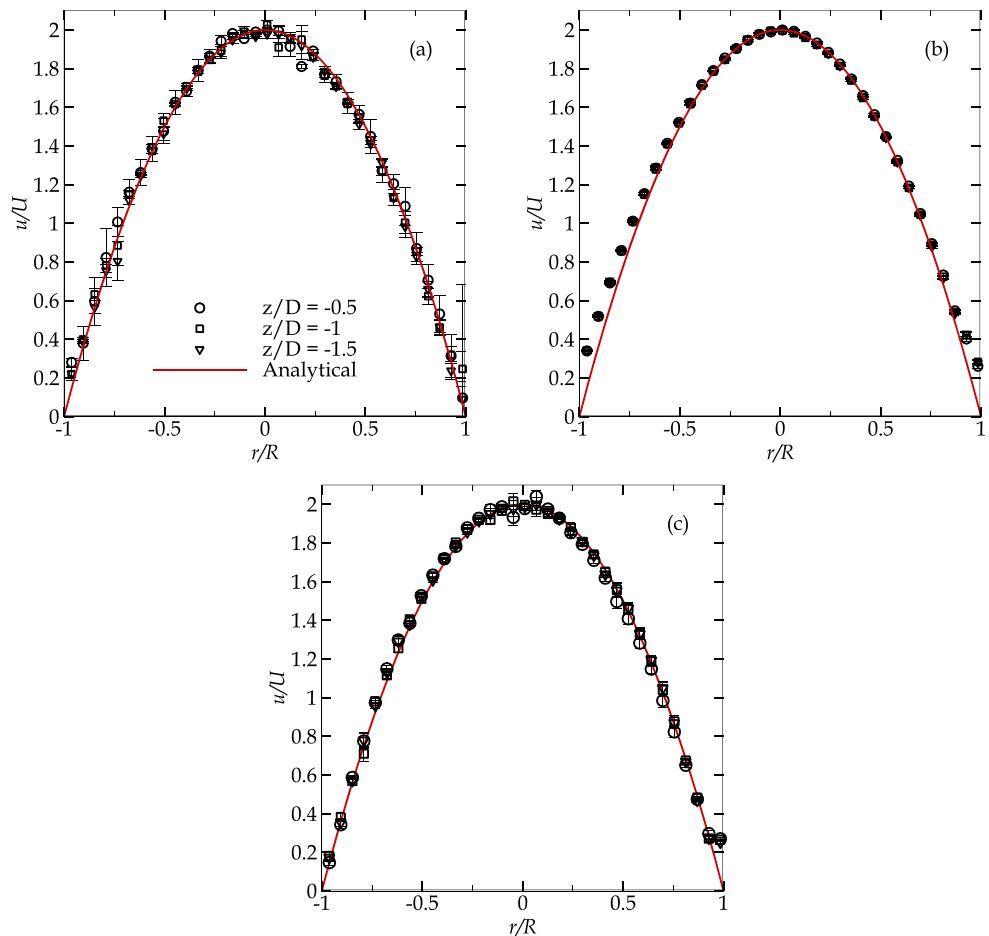
The radius of the plug region r_0 is reduced as the pressure is increased, since the wall shear stress increased with the

pressure, r_0 is a function of the wall shear stress, $r_0 = \tau_0 R / \tau_w$. The evolution of the axial velocity profiles for the Carbopol solutions is presented in Fig. 7(a)–(c). The decreasing of the radius r_0 is noticeable for high-pressure values and wall shear stress. The r_0 values were calculated using the relationship between wall shear stress and yield stress. The yield stress values obtained from the previous rheometric tests in CHPP geometry were employed to calculate the expected values for r_0 . Nevertheless, Fig. 7(d) shows that a noticeable difference in the r_0 values is presented when compared with the pressure measurement data. This discrepancy is a result of the slip behavior presented by the Carbopol solutions, where higher plug radii are visualized for low wall shear stress than expected from the $r_{0CHPP}/R = \tau_0/\tau_w$ relationship.

Validation stage

The laminar flow of Newtonian fluid represents the most straightforward case to solve using visualization techniques. Therefore, the validation of the PIV methodology was performed using the aqueous solution of 50 wt% glycerine as a Newtonian fluid (steady-state flow curve presented

Fig. 8 PIV methodology validation with Newtonian fluid. Comparison between the analytical solution and experimental data of the instantaneous velocity in the fully developed laminar regime for (a) $Re = 1$, (b) $Re = 10$, and (c) $Re = 160$



in Fig. 2). The instantaneous field of the axial velocity was calculated for three defined Reynolds numbers, $Re=1$, 10, and 100, by correlating pairs of images. The classical definition for the Reynolds number was applied for this validation stage $Re = \rho U D / \mu$, where U and μ are the mean velocity and the dynamic viscosity of the Newtonian fluid, respectively. Figure 8 compares the instantaneous axial velocity u , measured along the pipe diameter for three positions, and the analytical solution for Newtonian flow in the laminar regime. The results show a good agreement between the experimental and the analytical data for the three Reynolds cases, and the chosen parameters assure an excellent repeatability of the fluid flow phenomena. The highest deviation values are presented at the wall, reaching a maximal value of 12.7% for $Re=10$. Such a difference is due to the light refraction at this region of the test section, which affects the final correlation. Nevertheless, the error value is within an acceptable range for this technique. It is important to remark that our area of interest in the velocity profile is its central region, where a low refraction error is guaranteed. The error associated with the visualization technique for this validation stage is the same described

in “[Experimental setup and apparatus arrangement for visualization](#)”.

Shear stress and shear rate profiles

Figure 9 shows the linear shear stress distribution for each Carbopol solution for different pressure drops. The values were obtained by the experimental pressure drop measured at the test section and then were extrapolated along the pipe diameter using Eqs. 7 and 8. An increase of the τ_w ($r/R=1$ and $r/R=-1$) with the pressure drop is depicted for the three Carbopol solutions. The latter is expected as the polymeric material’s concentration increases, and higher pressure gradients are demanded to start and maintain the flow.

The shear rate values were obtained by applying the definition presented in Eq. 6 to the data obtained by the PIV technique. The shear rate distribution for each solution at different pressure drops values are presented in Fig. 10. As depicted for the shear stress distribution, the shear rate values at the wall boundaries increase with the pressure drop. The region near the wall decays in shear rate values when r/R reaches values higher than 0.8. This behavior suggests

Fig. 9 Shear stress distribution for fluids (a) C1, (b) C2, and (c) C3. The shear stress was obtained by measuring the pressure drop at the test section for laminar flow conditions

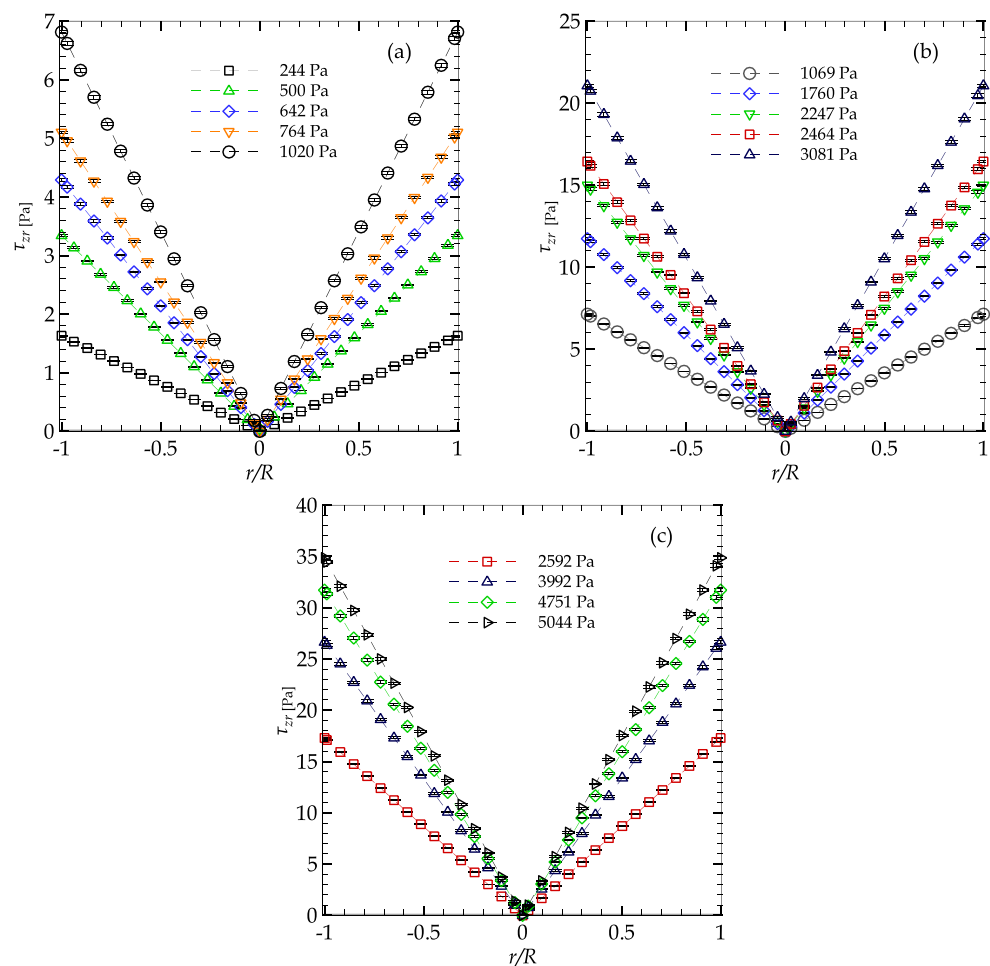
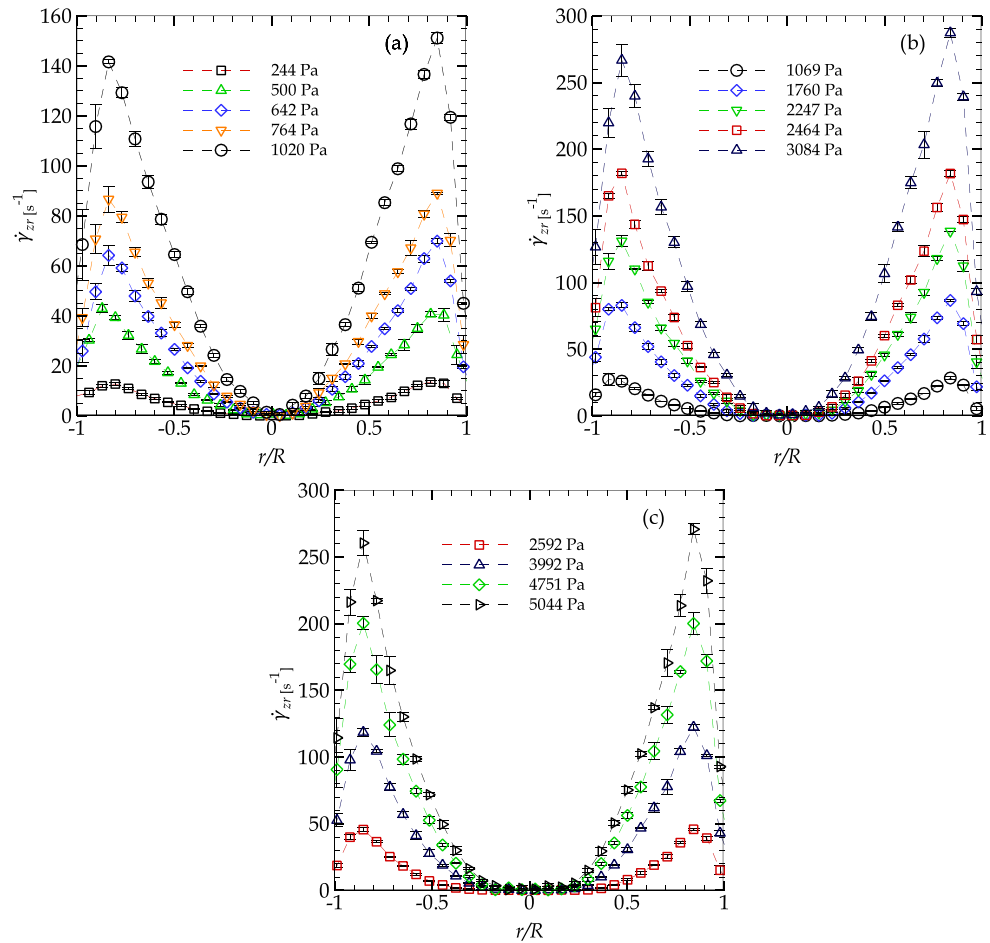


Fig. 10 Shear rate profiles were calculated by applying Eq. 6 to the values obtained with the IV correlations for velocity gradients at different pressure drop measurements for fluids (a) C1, (b) C2, and (c) C3, respectively



a layer under a sliding flow, as presented by the early studies of Coussot et al. (2009) and Park and Liu (2010).

Figure 11 shows a comparison of the shear rate profile between the three Carbopol solutions and the Newtonian fluid G50, flowing at the same Reynolds number, $Re=150$. The decaying of the shear rate profile near the wall, for $r/R > 0.8$, is not depicted for the Newtonian fluid, which seems to be a condition presented for fluids with shear thinning behavior.

Steady-state flow curve and Herschel-Bulkley model fit

New flow curves are calculated from the shear rate and the shear stress profiles presented in the last section. The flow curves fit by the Herschel-Bulkley model are depicted in Fig. 12(a). A shear stress value is related to a shear rate value for each position along the pipe diameter.

The flow curve is then reconstructed using the shear rate and shear stress distribution. The shear rate and shear stress values were limited to the regions out of the plug core region, where the shear rate values remain constant, and out of the layer near the wall, which seems to be under

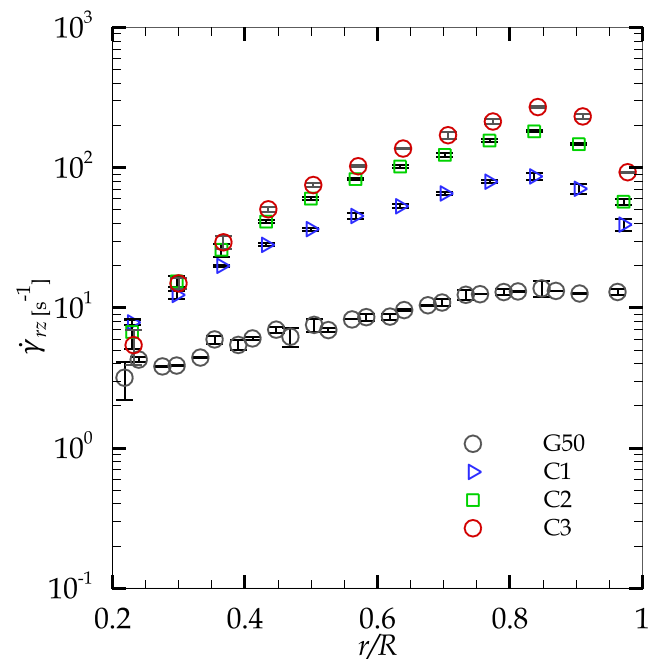
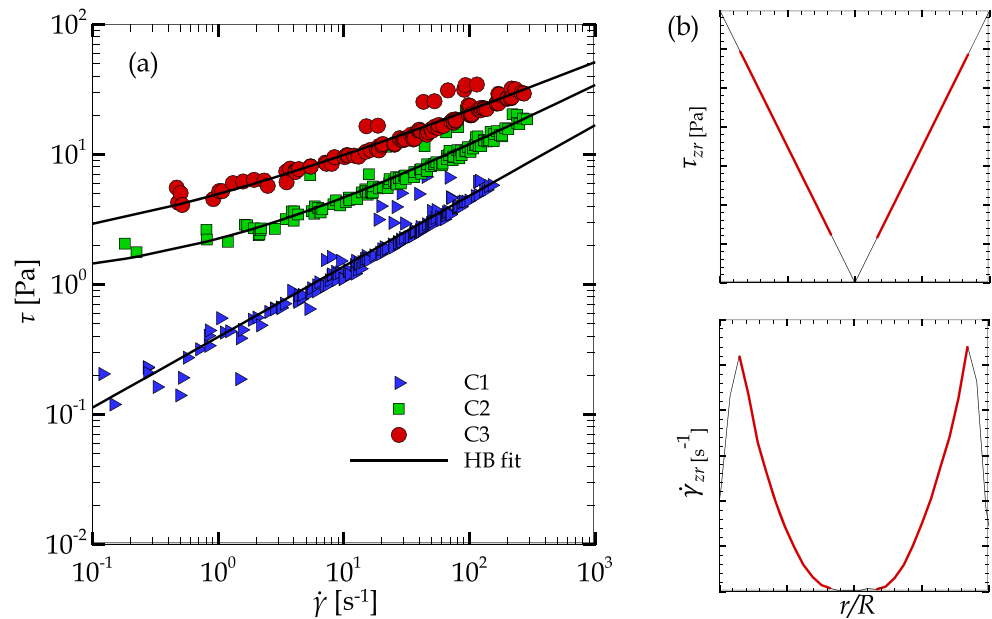


Fig. 11 Shear rate profiles are depicted for the three Carbopol solutions and the Newtonian fluid. The data were obtained for the same flow conditions, $Re=150$

Fig. 12 (a) Flow curve for the Carbopol solutions obtained from the shear stress and the shear rate distribution with Eqs. 6 and 7. The continuous line represents the fittings to the Herschel-Bulkley model. (b) Schema of the shear stress and shear rate values used to obtain the steady flow curve. The continuous red lines represent the range of the values validated for the flow curve extrapolation (values out of the slip and plug core regions)



sliding effects. The excluded regions can lead to a high deviation of the data and a misunderstanding of the shear stress behavior, as presented in different works that expose measurement mistakes related to the shear banding and slip conditions during the rheological analysis (Divoux et al. 2016; Andrade et al. 2020). Figure 12(b) depicts the region employed for the new flow curve calculation with red lines. Table 3 presents the parameters as a result of the fitting process by the Herschel-Bulkley (HB) model of the new flow curves. Lower values for τ_0 are obtained for the three solutions, as well as K and n values.

Figure 13 shows that the SCC geometry data follow the trend of the fitting flow curve obtained by the PIV shear rate calculations (SR), evidencing the presence of similar behavior in both geometries, between the pipe and the concentric cylinders, and could be associated with the presence of slippage at the wall boundaries. Such a condition is not presented in hatched geometry, as depicted in Fig. 13. The results suggest an overestimating

Herschel-Bulkley's parameter values in CHPP geometries for viscoplastic fluids when compare with pipe flow data.

For fluid C1, the τ_0 fitted value is 0, which reduces the general Herschel-Bulkley equation model to a Power-law (Oswald-de Waele) relationship, whose results differ from the initial values found by the CHPP geometry, suggesting that an erroneous description of fluid dynamics can be done, as the flow structure is strongly dependent on the parameters fitted by the rheological model.

Table 3 New flow fitted parameters were obtained by the Herschel-Bulkley model

Fluids	τ_0 [Pa]	K [Pa·s ^{<i>n</i>}]	n [–]
C1	0 ± 0.182	0.394 ± 0.100	0.543 ± 0.050
C2	1.05 ± 0.808	1.193 ± 0.409	0.481 ± 0.058
C3	1.506 ± 0.878	3.452 ± 1.233	0.386 ± 0.057

Data were obtained using the velocity gradients from the PIV methodology. The standard error values for all the fitted parameters result from the analysis of the residual values for a non-linear fitting process (Motulsky and Ransnas 1987)

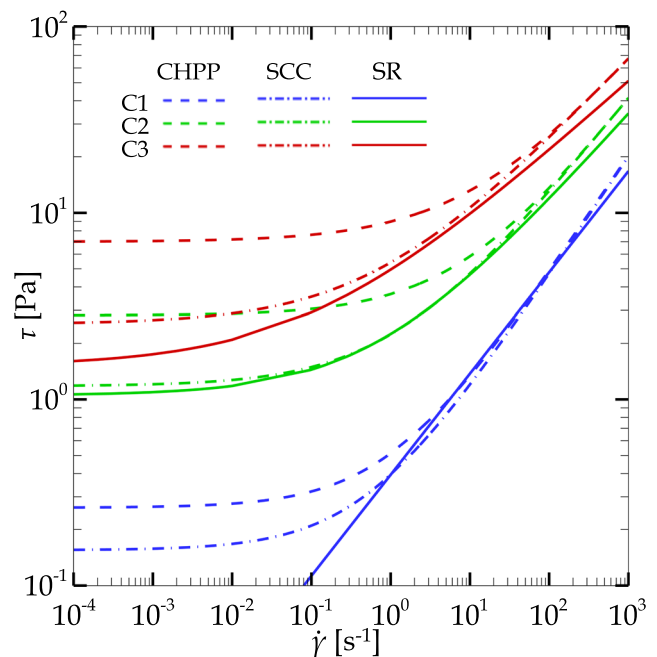


Fig. 13 Comparison of the steady-state flow curve for the three solutions performed for CHPP and SCC geometries and the fitted flow curve obtained by the shear strain calculations (SR)

It is interesting to remark that the differences found in the rheological parameters affect the flow regime calculation for each solution. Figure 14 compares the Reynolds number calculated with the parameters obtained for the CHPP geometry in the rheometer and the Reynolds number obtained by the shear rate calculations of the pipe flow with the PIV technique (SR) for the three shear-thinning solutions. The Reynolds number is calculated using the Malin’s (1998) expression for viscoplastic fluids

$$Re' = \frac{\rho \bar{U}^{(2-n)} D^n}{K(0.75 + 0.25/n)^n 8^{(n-1)}} \tag{10}$$

For low Reynolds numbers, it is noticeable a deviation higher than 10% between the Re'_{CHPP} and the Re'_{SR} in the range of 1 and 100. For Reynolds numbers above 100, the values lie within the deviation band of 10%; nevertheless, the difference increases for all the solutions as higher Reynolds numbers are demanded.

Plug and slip velocity

At first look, the slip velocity can be obtained directly from the velocity at the pipe wall. Nevertheless, this description is mere qualitative because any quantitative analysis is compromised by the low correlation and velocity gradient in this region. Figure 15 shows the axial velocity profile distribution near the pipe wall of the three Carbopol solutions for a $Re' \approx 100$. The velocity profiles are presented with the raw image of the seeding particles flowing along the pipe captured by the PIV high-speed

camera. A non-zero velocity is depicted at the pipe wall, and seems to increase with the Carbopol concentration and the wall shear stress; see the detailed region in Fig. 15, where the increase of the wall shear stress leads to a more stretched axial velocity profiles.

Therefore, the central region of the velocity profile is our main focus. In this region, the plug region for fluids with yield stress gives the maximal velocity value, and small variations of the local plug core velocity are depicted, which allows a better quantitative comparison of the velocities obtained by the different rheological measurements presented in this paper. Figure 16 shows the plug core velocity (U_p) as a function of the wall shear stress (τ_w). The U_p analytical values are calculated with the different rheological parameters: tests performed in the rheometer with the CHPP geometry and the rheological data obtained with the shear rate profiles (SR). Also, the experimental velocity values calculated directly with the PIV correlations (VP) are compared. The analytical values for U_p are calculated as (Chhabra and Richardson 2011; Peixinho et al. 2005)

$$U_p = \frac{nR}{(n + 1)} \left(\frac{\tau_w}{K} \right)^{1/n} \left(1 - \frac{\tau_0}{\tau_w} \right)^{(n+1)/n} \tag{11}$$

this equation also applies to the cases of null values for τ_0 .

A good agreement between the experimental data obtained directly from the velocity profiles and the shear rate profile measurements is depicted in Fig. 16 for U_p . On the contrary, the U_p values calculated by the rheological data with the CHPP geometry present the highest differences with the PIV experimental values.

The increases of the τ_w value lead to more significant differences in the U_p values between the rheometric and the pipe flow measurements in steady conditions. Therefore, using the plug core velocity, it is possible to achieve a macroscopic estimation of the slip velocity. Assuming the CHPP geometry avoids the slippage of the viscoplastic material with its wall surface, the slip velocity (U_s) is defined then as the difference between plug core velocity calculated by the fitting of the shear rate profiles (U_{PSR}) and the plug core velocity calculated with the CHPP rheometric data (U_{PCHPP}), $U_s = U_{PSR} - U_{PCHPP}$. Early studies defined U_s as a function of the wall shear stress for different polymers and suspensions, where a power model commonly represents the relationship (Kalyon 2005; Pérez-González et al. 2012; Poumaere et al. 2014)

$$U_s \propto \beta \tau^m \tag{12}$$

where $\beta = \frac{\delta}{K_s^{n_s}}$ is related to the slip layer δ , the slip consistency coefficient K_s and the slip behaviour index $m = 1/n_s$ of the fluid inside the slipping layers. This relationship was early proposed by Kalyon (2005)

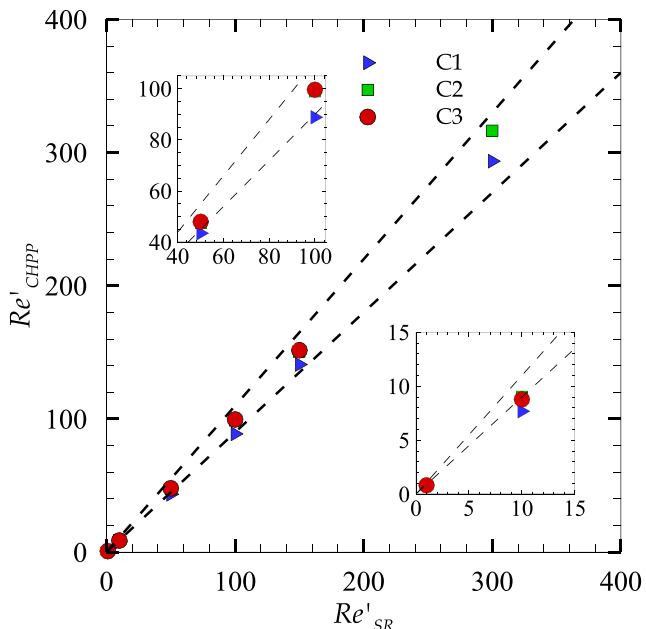


Fig. 14 Reynolds numbers comparison using the data fitted by the Herschel-Bulkley for data obtained from the rheometer tests and the data obtained from the shear rate distribution by the PIV technique

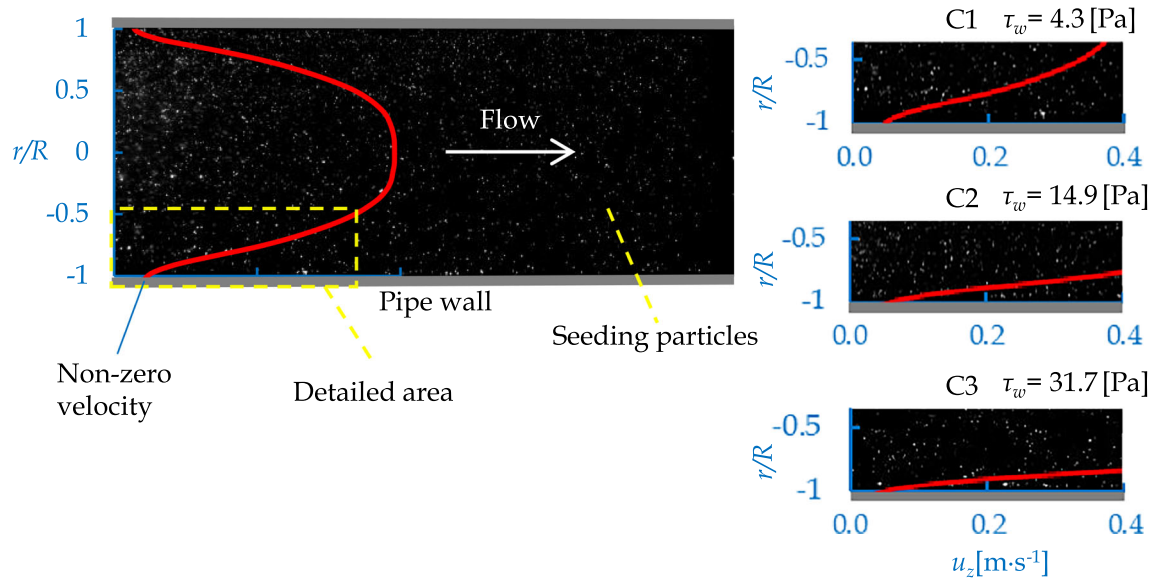


Fig. 15 Non-zero velocity is depicted at the pipe wall for the Carbopol solutions with $Re' \approx 10$. The region near the pipe wall is detailed, and an increase in the wall shear stress seems to affect the non-zero velocity. The horizontal axis shows the dimensional axial velocity

based on Bingham’s (1922) statements about the slip behavior. Figure 17 presents the behavior of this slip velocity as a function of the wall shear stress for the three Carbopol solutions, where a power scale is depicted from our experimental data. The power relationship given by $U_s \sim 5.47 \times 10^{-3} \tau_w^{1.26}$ presents a quasi-linear trend of the slip velocity with the wall shear stress; similar correlations

were exposed by Pérez-González et al. (2012), Poumaere et al. (2014), and Aktas et al. (2014), where the m value is also close to unity. This relationship is also consistent with the qualitative description previously presented in Fig. 15. The findings confirm the theory that the fluid

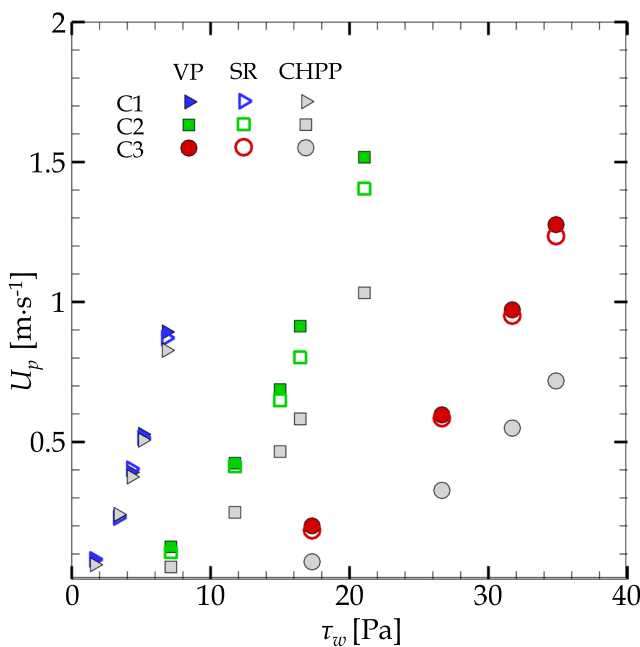


Fig. 16 Plug core velocity (U_p) as a function of the wall shear stress (τ_w) for each Carbopol solution. The U_p is presented for each measurement methodology: CHPP geometry in the rheometer, shear rate profiles (SR), and the velocity profiles data obtained directly from the PIV technique

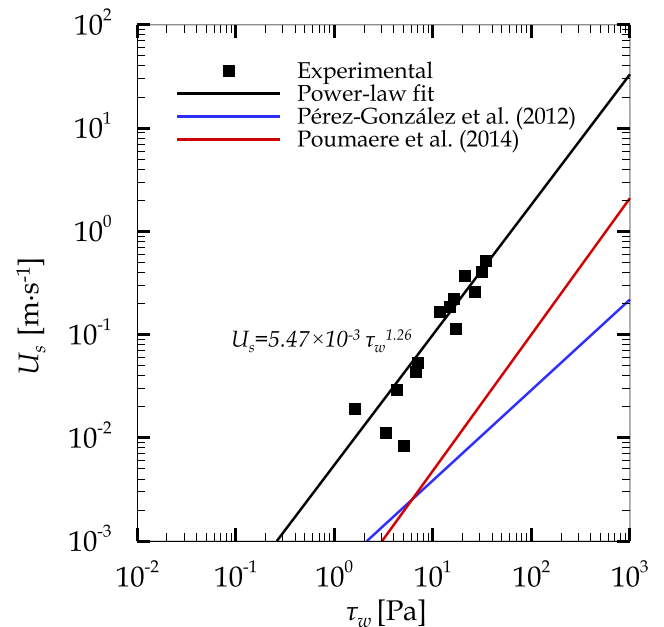


Fig. 17 Relationship of the slip velocity U_s with the wall shear stress τ_w . Experimental data were fitted by a Power-law model based on the Kalyon (2005) proposal expressed as $U_s \propto \beta \tau_w^m$. The red and solid blue lines are the Power-law models for the slip velocity obtained by Poumaere and Pérez-González, respectively. Pérez-González model is given by $\beta = 5.151e - 4$ and $m = 0.876$, and the Poumaere model is represented by $\beta = 2.3e - 4$ and $m = 1.32$

close to the wall presents Newtonian fluid characteristics, and its behavior shows the independence of the Carbopol fluid concentration. Our correlation is compared with the experimental fitting of the mentioned works of Pérez-González and Poumaere. The major discrepancy lay under the β value, explained by the different concentrations and the methodology used during the fluid preparation stage. These two factors strongly influence the final distribution of the micro-particles into the Carbopol solutions, which leads to different thicknesses of the shear layer δ .

Viscosity profiles were also obtained by the in situ approach of the viscoplastic fluid. The viscosity along the pipe diameter η_{rz} is defined by the Herschel-Bulkley model as following

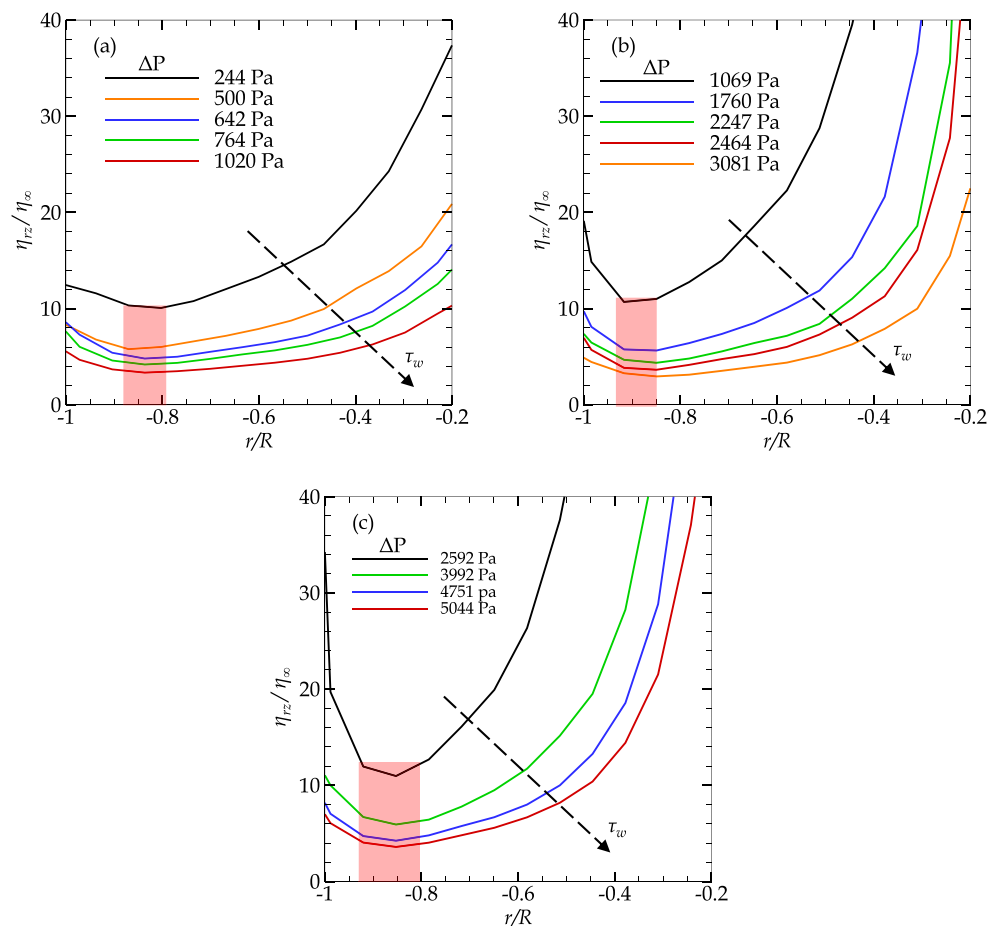
$$\eta_{rz} = \begin{cases} \tau_0 \dot{\gamma}_{rz}^{-1} + K \dot{\gamma}_{rz}^{n-1}, & \dot{\gamma}_{rz} < \dot{\gamma}_\infty \\ \eta_\infty, & \dot{\gamma}_{rz} \geq \dot{\gamma}_\infty \end{cases} \quad (13)$$

where the viscosity values were calculated using the fit parameters obtained for the Herschel-Bulkley model resumed in Table 3. The η_{rz} values were normalized by the viscosity η_∞ , which is the viscosity at $\dot{\gamma}_\infty$ ($\dot{\gamma}_{rz} \sim 2000s^{-1}$).

Figure 18 shows the changes in the viscosity profile with the increase of the driven pressure drop and the wall shear stress. It is interesting to remark that low wall shear stress values lead to a high viscosity gradient near the pipe wall and high viscosity values at the wall. These marked viscosity variations present low U_s values, as depicted in Fig. 17. Such behavior reinforces the idea that the higher slip velocities are depicted as nearer to the Newtonian behavior in the fluid layer near the pipe wall. The latter could also be sustained by the differences in the flow behavior presented in the fluid layers; as these layers reach the pipe wall, a disruption in the propagation of the shear rate is presented. Such disruptions are highlighted with a red region in Fig. 18, where η_{rz}/η_∞ reaches the local minima value and then increases until the pipe wall. These minima values are presented due to the shear rate in this region depicting higher values.

To conclude this subsection, we observe during the flow of polymer solutions, such as Carbopol ones, that the slip behavior is an inherent condition of this material. The slipping condition is then strongly dependent on its composition and the interaction between the fluid layers during an imposed pressure-driven flow.

Fig. 18 Dimensionless viscosity profiles η_{rz}/η_∞ plotted in the dimensionless radial coordinate. The η_{rz}/η_∞ profiles are presented for different driven pressure drops (wall shear stress). The red regions depict the variation of the η_{rz}/η_∞ gradient near the pipe wall



Conclusions

The PIV measurements were employed to estimate a new flow curve for three different Carbopol solutions. Using correlations of the velocity gradients calculations to obtain shear rate profiles along a test section for a pipe flow, and supported with pressure drop and shear wall stress measurements to calculate shear stress-shear rate relationships. The application demonstrated that the Herschel Bulkley model's parameters obtained from rheometric measurements can differ from in situ techniques due to the geometrical aspect differences and the presence of inherent behaviors related to the micro-structural interactions as the slipping velocity presented at the pipe wall. Such as condition is not considered in a controlled performance in the rheometer. A wrong interpretation of the hydrodynamic behavior can be made with results from a rheometer performance due to the direct influence of the rheological parameters in the viscoplastic fluid behavior. Also, it was proved that with the present methodology is possible to provide a reliable macro-description of the slip velocity U_s values for different wall shear stress, presenting good agreement when compared with early experimental works focused on the study of the slip behavior in polymers by a micro-scale approach.

As a final remark, we expect this in situ rheological technique to be extended for studying and comprehending other complex materials such as thixotropic and viscoelastic fluids, furnishing a better description of realistic actual transporting conditions in pipe flow geometries.

Acknowledgements The authors thank the Multilab LabReo-CERNN/UTFPR for providing the rheometers used in the current work.

Funding The authors acknowledge the financial support of PETROBRAS S/A (TC 0050.0070318.11.9) as also the Coordination for the Improvement of Higher Education Personnel - Brazil (CAPES) - Finance Code 001, and the Brazilian National Council for Scientific and Technological Development (CNPq).

References

- Aktas S, Kalyon DM, Marín-santibáñez BM, et al. (2014) Shear viscosity and wall slip behavior of a viscoplastic hydrogel. *J Rheol* 58(2):513–535. <https://doi.org/10.1122/1.4866295>
- Andrade DE, Fernandes RR, Santos TG, et al. (2016) Curve-fitting equation for prediction of the start-up stress overshoot of an oil-based drilling fluid. *J Pet Sci Eng* 146:902–908. <https://doi.org/10.1016/j.petrol.2016.07.037>
- Andrade DE, Ferrari M, Coussot P (2020) The liquid regime of waxy oils suspensions: a magnetic resonance velocimetry analysis. *J Non-Newtonian Fluid Mech* 279:104:261. <https://doi.org/10.1016/j.jnnfm.2020.104261>
- Bingham EC (1922) Fluidity and plasticity vol 2. McGraw-Hill, New York
- Bonn D, Denn MM, Berthier L et al (2017) Yield stress materials in soft condensed matter. *Rev Modern Phys* 89(3):035,005. <https://doi.org/10.1103/RevModPhys.89.035005>
- Bourgoyne Jr AT, Millheim KK, Chenevert ME, et al. (1986) Applied drilling engineering. Volume 2. Society of Petroleum Engineers, Richardson. <https://www.osti.gov/biblio/5050497>
- Caenn R, Darley HC, Gray GR (2011) Composition and properties of drilling and completion fluids. Gulf professional publishing, Cambridge. <https://doi.org/10.1016/C2015-0-04159-4>
- Cheng DC (1986) Yield stress: a time-dependent property and how to measure it. *Rheol Acta* 25(5):542–554. <https://doi.org/10.1007/BF01774406>
- Chhabra RP, Richardson JF (2011) Non-Newtonian flow and applied rheology: engineering applications. Butterworth-Heinemann
- Chun MK, Choi HK (2004) Preparation and characterization of enrofloxacin/carbopol complex in aqueous solution. *Arch Pharm Res* 27(6):670–675. <https://doi.org/10.1007/BF02980168>
- Coussot P, Nguyen QD, Huynh H et al (et al.) Viscosity bifurcation in thixotropic, yielding fluids. *J Rheol* 46(3):573–589. <https://doi.org/10.1122/1.1459447>
- Coussot P, Tocquer L, Lanos C, et al. (2009) Macroscopic vs. local rheology of yield stress fluids. *J Non-Newtonian Fluid Mech* 158(1-3):85–90. <https://doi.org/10.1016/j.jnnfm.2008.08.003>
- De Graef V, Depypere F, Minnaert M, et al. (2011) Chocolate yield stress as measured by oscillatory rheology. *Food Res Int* 44(9):2660–2665. <https://doi.org/10.1016/j.foodres.2011.05.009>
- Di Giuseppe E, Corbi F, Funicello F, et al. (2015) Characterization of carbopol® for hydrogel rheology for experimental tectonics and geodynamics. *Tectonophysics* 642:29–45. <https://doi.org/10.1016/j.tecto.2014.12.005>
- Dimitriou CJ, McKinley GH, Venkatesan R (2011) Rheo-piv analysis of the yielding and flow of model waxy crude oils. *Energy Fuels* 25(7):3040–3052. <https://doi.org/10.1021/ef2002348>
- Divoux T, Fardin MA, Manneville S, et al. (2016) Shear banding of complex fluids. *Ann Rev Fluid Mech* 48:81–103. <https://doi.org/10.1146/annurev-fluid-122414-034416>
- Dusunceli N, Colak OU (2008) The effects of manufacturing techniques on viscoelastic and viscoplastic behavior of high density polyethylene (hdpe). *Mater Des* 29(6):1117–1124. <https://doi.org/10.1016/j.matdes.2007.06.003>
- Fernandes R, Suleiman N, Wilson D (2021) In-situ measurement of the critical stress of viscoplastic soil layers. *J Food Eng* 303:110,568. <https://doi.org/10.1016/j.jfoodeng.2021.110568>
- Fernandes RR, Andrade DE, Franco AT, et al. (2017a) Influence of pre-shearing on rheometric measurements of an oil-based drilling fluid. *Rheol Acta* 56(9):743–752. <https://doi.org/10.1007/s00397-017-1027-y>
- Fernandes RR, Andrade DE, Franco AT, et al. (2017b) The yielding and the linear-to-nonlinear viscoelastic transition of an elasto-viscoplastic material. *J Rheol* 61(5):893–903. <https://doi.org/10.1122/1.4991803>
- Fernandes RR, Turezo G, Andrade DE, et al. (2019) Are the rheological properties of water-based and synthetic drilling fluids obtained by the fann 35a viscometer reliable? *J Pet Sci Eng* 177:872–879. <https://doi.org/10.1016/j.petrol.2019.02.063>
- García-Blanco YJ, Mancilla E, Germer EM, et al. (2021) A piv investigation of laminar and turbulent viscoplastic fluid flow on axisymmetric abrupt contraction. *Fluid Dyn Res* 53(5):055,501. <https://doi.org/10.1088/1873-7005/ac2481>
- Ghàitanellis A, Violeau D, Ferrand M, et al. (2018) A sph elastic-viscoplastic model for granular flows and bed-load transport. *Adv Water Resour* 111:156–173. <https://doi.org/10.1016/j.advwatres.2017.11.007>
- Jiang T, Young A, Metzner A (1986) The rheological characterization of hpg gels: measurement of slip velocities in capillary tubes. *Rheologica acta* 25(4):397–404. <https://doi.org/10.1007/BF01331511>

- Kalyon DM (2005) Apparent slip and viscoplasticity of concentrated suspensions. *J Rheol* 49(3):621–640. <https://doi.org/10.1122/1.1879043>
- Kalyon DM, Yaras P, Aral B, et al. (1993) Rheological behavior of a concentrated suspension: a solid rocket fuel simulant. *J Rheol* 37(1):35–53. <https://doi.org/10.1122/1.550435>
- Katritsis D, Kaiktsis L, Chaniotis A, et al. (2007) Wall shear stress: theoretical considerations and methods of measurement. *Prog Cardiovasc Dis* 49(5):307–329. <https://doi.org/10.1016/j.pcad.2006.11.001>
- Kim JY, Song JY, Lee EJ, et al. (2003) Rheological properties and microstructures of carbopol gel network system. *Colloid Polym Sci* 281(7):614–623. <https://doi.org/10.1007/s00396-002-0808-7>
- Koponen A, Haavisto S, Salmela J, et al. (2019) Slip flow and wall depletion layer of microfibrillated cellulose suspensions in a pipe flow. *Ann Trans Nord Soc Rheol* 27:13–20
- Li T, Wolcott M (2005) Rheology of wood plastics melt. part 1. capillary rheometry of hdpe filled with maple. *Polym Eng Sci* 45(4):549–559. <https://doi.org/10.1002/pen.20308>
- Longo GA, Zilio C (2011) Experimental measurement of thermophysical properties of oxide–water nano-fluids down to ice-point. *Exp Thermal Fluid Sci* 35(7):1313–1324. <https://doi.org/10.1016/j.expthermflusci.2011.04.019>
- Macosko CW (1994) Rheology: principles, measurements and applications. Wiley, New York
- Mahto V, Sharma V (2004) Rheological study of a water based oil well drilling fluid. *J Pet Sci Eng* 45(1-2):123–128. <https://doi.org/10.1016/j.petrol.2004.03.008>
- Malin M (1998) Turbulent pipe flow of herschel-bulkley fluids. *Int Commun Heat Mass Transfer* 25(3):321–330. [https://doi.org/10.1016/S0735-1933\(98\)00019-0](https://doi.org/10.1016/S0735-1933(98)00019-0)
- Marín-Santibáñez BM, Pérez-González J, Gómez-Herrera G, et al. (2020) Capillary extrusion of polypropylene/high-density polyethylene immiscible blends as studied by rheo-particle image velocimetry. *Polym Test* 84:106,390. <https://doi.org/10.1016/j.polymertesting.2020.106390>
- Medina-Bañuelos EF, Marín-santibáñez BM, Pérez-González J (2022) Rheo-piv analysis of the steady torsional parallel-plate flow of a viscoplastic microgel with wall slip. *J Rheol* 66(1):31–48. <https://doi.org/10.1122/8.0000310>
- Mendes R, Vinay G, Coussot P (2017) Yield stress and minimum pressure for simulating the flow restart of a waxy crude oil pipeline. *Energy Fuels* 31(1):395–407. <https://doi.org/10.1021/acs.energyfuels.6b02576>
- Mika L (2012) Rheological behaviour of low fraction ice slurry in pipes and pressure loss in pipe sudden contractions and expansions. *Int J Refrig* 35(6):1697–1708. <https://doi.org/10.1016/j.ijrefrig.2012.05.001>
- Motulsky HJ, Ransnas LA (1987) Fitting curves to data using nonlinear regression: a practical and nonmathematical review. *FASEB J* 1(5):365–374. <https://doi.org/10.1096/fasebj.1.5.3315805>
- Muramatsu M, Kanada K, Nishida A, et al. (2000) Application of carbopol® to controlled release preparations i. carbopol® as a novel coating material. *Int J Pharm* 199(1):77–83. [https://doi.org/10.1016/S0378-5173\(00\)00374-4](https://doi.org/10.1016/S0378-5173(00)00374-4)
- de Oliveira GM, Negrao CO (2015) The effect of compressibility on flow start-up of waxy crude oils. *J Non-Newtonian Fluid Mech* 220:137–147. <https://doi.org/10.1016/j.jnnfm.2014.12.010>
- Park YS, Liu PLF (2010) Oscillatory pipe flows of a yield-stress fluid. *J Fluid Mech* 658:211–228. <https://doi.org/10.1017/S0022112010001667>
- Peixinho J, Nouar C, Desaubry C, et al. (2005) Laminar transitional and turbulent flow of yield stress fluid in a pipe. *J Non-Newtonian Fluid Mech* 128(2-3):172–184. <https://doi.org/10.1016/j.jnnfm.2005.03.008>
- Pérez-González J, López-Durán JJ, Marín-santibáñez BM, et al. (2012) Rheo-piv of a yield-stress fluid in a capillary with slip at the wall. *Rheol Acta* 51(11-12):937–946. <https://doi.org/10.1007/s00397-012-0651-9>
- Piau JM (2007) Carbopol gels: elastoviscoplastic and slippery glasses made of individual swollen sponges: meso-and macroscopic properties, constitutive equations and scaling laws. *J Non-Newtonian Fluid Mech* 144(1):1–29. <https://doi.org/10.1016/j.jnnfm.2007.02.011>
- Poumaere A, Moyers-González M, Castelain C, et al. (2014) Unsteady laminar flows of a carbopol® gel in the presence of wall slip. *J Non-Newtonian Fluid Mech* 205:28–40. <https://doi.org/10.1016/j.jnnfm.2014.01.003>
- Quitian LH, Andrade DE, Franco AT (2022) Bentonite-free water-based drilling fluids at hp/ht condition: a rheometric analysis. *Rheol Acta* :1–15. <https://doi.org/10.1007/s00397-022-01356-x>
- Raffel M, Willert CE, Kompenhans J, et al. (1998) Particle image velocimetry: a practical guide, vol 2. Springer, New York. <https://doi.org/10.1007/978-3-319-68852-7>
- Reuss DL, Adrian RJ, Landreth CC, et al. (1989) Instantaneous planar measurements of velocity and large-scale vorticity and strain rate in an engine using particle-image velocimetry. *SAE Transactions*:1116–1141. <https://www.jstor.org/stable/44581012>
- Schmidt M, Wassner E, Münstedt H (1999) Setup and test of a laser doppler velocimeter for investigations of flow behaviour of polymer melts. *Mech Time-Dependent Mater* 3(4):371–393. <https://doi.org/10.1023/A:1009820500869>
- Shamu TJ, Zou L, Kotzé R, et al. (2020) Radial flow velocity profiles of a yield stress fluid between smooth parallel disks. *Rheol Acta* 59(4):239–254. <https://doi.org/10.1007/s00397-020-01203-x>
- Sobamowo G, Akinshilo A, Yinusa A, et al. (2018) Nonlinear slip effects on pipe flow and heat transfer of third grade fluid with nonlinear temperature-dependent viscosities and internal heat generation. *Software Eng* 6(3):69–88. <https://doi.org/10.11648/j.se.20180603.11>
- Tanner RI (2000) Engineering rheology, vol 52. OUP Oxford, Oxford
- Turian RM, Yuan TF (1977) Flow of slurries in pipelines. *AIChE J* 23(3):232–243. [https://doi.org/10.1016/S0301-9322\(97\)00039-6](https://doi.org/10.1016/S0301-9322(97)00039-6)
- Westerweel J, Draad A, Van der Hoeven JT, et al. (1996) Measurement of fully-developed turbulent pipe flow with digital particle image velocimetry. *Exp Fluids* 20(3):165–177. <https://doi.org/10.1007/BF00190272>
- Wilms P, Wieringa J, Blijdenstein T, et al. (2020) Wall slip of highly concentrated non-brownian suspensions in pressure driven flows: a geometrical dependency put into a non-newtonian perspective. *J Non-Newtonian Fluid Mech* 282:104,336. <https://doi.org/10.1016/j.jnnfm.2020.104336>
- Yoshimura A, Prud'homme RK (1988) Wall slip corrections for couette and parallel disk viscometers. *J Rheol* 32(1):53–67. <https://doi.org/10.1122/1.549963>
- Younes E, Himl M, Stary Z, et al. (2021) In-situ visualisation of the micro-structure of a carbopol gel during a confined microscopic

- flow. *J Non-Newtonian Fluid Mech* 296:104,630. <https://doi.org/10.1016/j.jnnfm.2021.104630>
- Zhang X, Lorenceau E, Bourouina T, et al. (2018) Wall slip mechanisms in direct and inverse emulsions. *J Rheol* 62(6):1495–1513. <https://doi.org/10.1122/1.5046893>
- Zhu H, Kim Y, De Kee D (2005) Non-newtonian fluids with a yield stress. *J Non-Newtonian Fluid Mech* 129(3):177–181. <https://doi.org/10.1016/j.jnnfm.2005.06.001>

Publisher's note Springer Nature remains neutral with regard to jurisdictional claims in published maps and institutional affiliations.

Springer Nature or its licensor (e.g. a society or other partner) holds exclusive rights to this article under a publishing agreement with the author(s) or other rightsholder(s); author self-archiving of the accepted manuscript version of this article is solely governed by the terms of such publishing agreement and applicable law.

Affiliations

Yamid J. García-Blanco¹  · Vitor Y. Urazaki¹ · Ángel. D. J. Rivera¹  · Luis H. Quitian¹  ·
Eduardo M. Germer¹  · Admilson T. Franco¹ 

Vitor Y. Urazaki
vitura.1998@alunos.utfpr.edu.br

Ángel. D. J. Rivera
angeljimenez@alunos.utfpr.edu.br

Luis H. Quitian
luis.2019@alunos.utfpr.edu.br

Eduardo M. Germer
eduardomg@utfpr.edu.br

¹ Research Center for Rheology and Non-Newtonian Fluids–CERNN, Post-graduate Program in Mechanical and Materials Engineering–PPGEM, Federal University of Technology-Paraná– UTFPR, Rua Dep. Heitor Alencar Furtado, 5000 - Bloco N - Ecoville, Curitiba, 81280-340, Paraná, Brazil